



HAL
open science

Simulation of Seismic Wave Propagation on Asteroid Ryugu Induced by The Impact Experiment of The Hayabusa2 Mission: Limited Mass Transport by Low Yield Strength of Porous Regolith

G. Nishiyama, T. Kawamura, N. Namiki, B. Fernando, K. Leng, K. Onodera, S. Sugita, T. Saiki, H. Imamura, Y. Takagi, et al.

► **To cite this version:**

G. Nishiyama, T. Kawamura, N. Namiki, B. Fernando, K. Leng, et al.. Simulation of Seismic Wave Propagation on Asteroid Ryugu Induced by The Impact Experiment of The Hayabusa2 Mission: Limited Mass Transport by Low Yield Strength of Porous Regolith. *Journal of Geophysical Research. Planets*, 2021, 126, 25 pp. 10.1029/2020JE006594 . insu-03590095

HAL Id: insu-03590095

<https://insu.hal.science/insu-03590095>

Submitted on 3 Mar 2022

HAL is a multi-disciplinary open access archive for the deposit and dissemination of scientific research documents, whether they are published or not. The documents may come from teaching and research institutions in France or abroad, or from public or private research centers.

L'archive ouverte pluridisciplinaire **HAL**, est destinée au dépôt et à la diffusion de documents scientifiques de niveau recherche, publiés ou non, émanant des établissements d'enseignement et de recherche français ou étrangers, des laboratoires publics ou privés.

Copyright

JGR Planets

RESEARCH ARTICLE

10.1029/2020JE006594

[†]Yuichi Iijima passed away in December 2012. Chisato Okamoto passed away in July 2018.

Key Points:

- Unexpectedly little movement of boulders due to the Small Carry-on Impactor impact experiment on Ryugu is investigated by seismic wave propagation simulation
- Low-yield strength of asteroid regolith is likely to limit seismic wave amplitude
- Meteoroid impacts on small asteroids possibly cause seismic shaking, but its contribution to resurfacing is localized

Supporting Information:

- Supporting Information S1
- Table S1

Correspondence to:

G. Nishiyama,
gaku.nishiyama@eps.s.u-tokyo.ac.jp

Citation:

Nishiyama, G., Kawamura, T., Namiki, N., Fernando, B., Leng, K., Onodera, K., et al. (2021). Simulation of seismic wave propagation on asteroid Ryugu induced by the impact experiment of the Hayabusa2 mission: Limited mass transport by low yield strength of porous regolith. *Journal of Geophysical Research: Planets*, 126, e2020JE006594. <https://doi.org/10.1029/2020JE006594>

Received 26 JUN 2020

Accepted 1 DEC 2020

Author Contributions:

Conceptualization: T. Kawamura
Data curation: S. Sugita, T. Saiki, H. Imamura, Y. Takagi, H. Yano, M. Hayakawa, C. Okamoto, H. Sawada, Y. Tsuda, K. Ogawa, S. Nakazawa, Y. Iijima
Formal analysis: G. Nishiyama
Investigation: G. Nishiyama
Methodology: B. Fernando, K. Leng
Project Administration: T. Saiki, H. Imamura, H. Sawada, Y. Tsuda, S. Nakazawa, Y. Iijima

Simulation of Seismic Wave Propagation on Asteroid Ryugu Induced by The Impact Experiment of The Hayabusa2 Mission: Limited Mass Transport by Low Yield Strength of Porous Regolith

G. Nishiyama¹ , T. Kawamura² , N. Namiki^{3,4} , B. Fernando⁵ , K. Leng⁵ , K. Onodera^{2,4,6} , S. Sugita^{1,7} , T. Saiki⁶ , H. Imamura⁶ , Y. Takagi⁸ , H. Yano^{6,4} , M. Hayakawa⁶ , C. Okamoto^{9,†} , H. Sawada⁶ , Y. Tsuda⁶ , K. Ogawa^{10,9} , S. Nakazawa⁶ , and Y. Iijima^{6,†} 

¹Department of Earth and Planetary Science, The University of Tokyo, Tokyo, Japan, ²Institut de Physique du Globe de Paris, Université de Paris, Paris, France, ³National Astronomical Observatory of Japan, Mitaka, Japan, ⁴The Graduate University for Advanced Studies, SOKENDAI, Hayama, Japan, ⁵University of Oxford, Oxford, UK, ⁶Institute of Space and Astronautical Science, Japan Aerospace Exploration Agency, Sagami-hara, Japan, ⁷Research Center of the Early Universe, The University of Tokyo, Tokyo, Japan, ⁸Aichi Toho University, Nagoya, Japan, ⁹Kobe University, Kobe, Japan, ¹⁰JAXA Space Exploration Center, Japan Aerospace Exploration Agency, Sagami-hara, Japan

Abstract Seismic shaking has been regarded as an essential source of resurfacing on asteroids. The Small Carry-on Impactor (SCI) operation on Hayabusa2 has been expected to be a unique opportunity for testing in situ seismic shaking whose energy is sufficiently large to excite observable surface modification. However, no obvious regolith hopping was identified even immediately outside of the crater formed by the SCI impact. To understand this discrepancy from the expectation, we simulate seismic wave propagation on Ryugu with a wide range of surface material properties and evaluate maximum acceleration on the surface. Numerical results reveal that low-quality factor or low seismic efficiency is required to explain the lack of geomorphological change after the SCI experiment. Considering that scattering under anhydrous conditions cannot efficiently dissipate energy, such a low-quality factor is not plausible. The weak yield strength in porous materials can efficiently decrease seismic wave energies, making the apparent seismic efficiency extremely low. Based on this hypothesis, we propose a formulation of surface mobility on asteroids that considers the physical properties of regolith. We consistently estimate the occurrence of seismic shaking with the existence of unstable boulders on Ryugu.

Plain Language Summary The Japanese asteroid exploration mission, Hayabusa2, successfully performed an artificial impact cratering operation on April 5, 2019. Extensive surface modification was expected to be excited by the impact-induced seismic waves; however, boulders stayed at almost the same location. We conduct seismic wave propagation simulations to resolve this apparent discrepancy and to understand the physical properties of Ryugu. We show that surface changes are strongly dependent on a shallow subsurface. Our results suggest that the conversion of impact energy to seismic waves is less efficient than previously thought. The weakness of powdery regolith may limit asteroid-quakes at the surface. Based on this hypothesis, we propose a formulation how the surface moves on asteroids that considers the unclear properties of regolith. The lack of seismic shaking agrees with the mysterious discovery that boulders stay unstably on other boulders.

1. Introduction

Multiple space exploration missions have recently revealed that asteroids have complex and variable surfaces. Geomorphological features are clues for mass transport processes occurring on small bodies. For example, the NEAR Shoemaker mission discovered a loose regolith layer on asteroid Eros. There are direct evidences of downslope motions, such as flat-floored sediment ponds in craters, a deficit of small craters, and large blocks surrounded by debris aprons (e.g., Thomas et al., 2002; Veverka et al., 2001). Miyamoto et al. (2007) report from images taken by Hayabusa that the surface regolith on Itokawa is segregated. However, transporting processes of asteroid regolith in both lateral and vertical directions remain ambiguous.

Supervision: T. Kawamura, N. Namiki, S. Sugita

Validation: G. Nishiyama, K. Onodera

Writing – original draft: G. Nishiyama, T. Kawamura, N. Namiki

Thus, variable surface renewal processes must be clarified to interpret resurfacing and collisional history from crater density and samples returned by the spacecraft.

Although many renewal processes have been proposed (e.g., Colwell et al., 2005), global vibration, in other words, impact-induced seismic shaking, has been regarded to be the most efficient for the mass transport of asteroid regolith (e.g., Richardson et al., 2004). Once a meteoroid hits an asteroid, a small fraction of the kinetic energy of the impactor is converted to seismic waves, which generate ground acceleration on the surface of asteroid. The gravity of asteroids typically ranges from 10^{-5} to 10^{-3} that of the Earth. Therefore, seismic acceleration easily overcomes the gravity and excites asteroid resurfacing through regolith sliding and dust lofting. Furthermore, in the case of asteroid-quakes, energy is confined in a much smaller volume than with earthquakes or moonquakes, therefore seismic shaking becomes effective. For example, Garcia et al. (2015) numerically show that even a 10-g micrometeoroid collision at a speed of 6 km/s sufficiently excites global seismic shaking on kilometeric scale asteroids. Through laboratory experiments, Yasui et al. (2015) reveal that the impact of a 0.1-g stainless steel projectile at a speed of ~ 100 m/s can provoke a seismic acceleration outside craters ~ 10 times larger than Earth's gravity. Although several numerical and experimental studies have been performed that assume seismic wave propagation in an elastic medium, the effect of powdery material under microgravity on wave propagation is not understood. We focus on these points and carefully examine to what extent elastic wave propagation can be applied for powdery asteroid regolith.

The Japanese spacecraft, Hayabusa2, which explored the near-earth asteroid 162173 Ryugu from June 2018 to November 2019, was planned to investigate in situ seismic shaking (Arakawa et al., 2017). Included in the Hayabusa2 payload was a Small Carry-on Impactor (SCI), which generates an artificial crater to bring fresh samples back to the Earth. The SCI experiment aimed to investigate subsurface properties and to study the crater formation process on an actual asteroid surface. The SCI experiment can also be regarded as an active seismic experiment (Arakawa et al., 2017), although there are no seismometers placed on the asteroid. Instead, images of the impact site before and after the SCI experiment were taken by Optical Navigation Camera (ONC) (Kameda et al., 2015, 2017), allowing the measurement of boulder movement by comparing two sets of images. Because the impact energy of SCI was sufficiently large, the surface morphology was predicted to be modified due to regolith movement (Arakawa et al., 2017).

In April 2019, the SCI operation was successfully conducted, and a Deployable CAMera 3 (DCAM3) provided images during crater formation (Arakawa et al., 2020). Hayabusa2 took images of the periphery of the SCI crater to be compared with the topography before the SCI impact (Figure 1). The impactor formed a crater with an ~ 17 -m rim diameter, and ejecta was deposited more than 40 m from the center of the crater. The comparison of these images clearly illustrates that boulders outside of or adjacent to the edge of the crater did not move more than 1 m.

We aim to understand this unexpected immobility of boulders and to identify physical properties that control seismic shaking on asteroids. For this purpose, we conduct seismic wave propagation simulations with a wide range of parameters, including rigidities, quality factors and, seismic efficiencies. Our simulation results cannot be applied to the region of plastic deformation. However, permanent deformation appears to be confined within the inside of the SCI crater and its close surroundings (Figure 1). Therefore, wave propagation outside of the SCI crater is assumed to be elastic in this study. Also, we note that ejecta curtain growth is a different process from surface modification due to seismic waves. Arakawa et al. (2020) show that more than 100 s were required for the growth of the ejecta curtain. If ejection process were related with seismic waves, the expected seismic velocity would be smaller by three orders of magnitude than that expected from lunar regolith. Additionally, Yasui et al. (2015) indicate the period of time for crater formation is much longer than the excitation of the seismic wave. By using the 1-m upper bound on the boulder movement, we constrain the elastic properties of rubble-pile asteroid Ryugu and the characteristics of powdery regolith behavior. Then, we discuss the anelastic effects of powdery regolith and the surface mobility of various impacts.

2. Seismic Wave Propagation Modeling

2.1. Numerical Code

We apply the AxiSEM3D code developed by Leng et al. (2016) to the asteroid. This simulation code employs spectrum elemental method and enables fast 3D global seismic wave propagation modeling. The Ax-

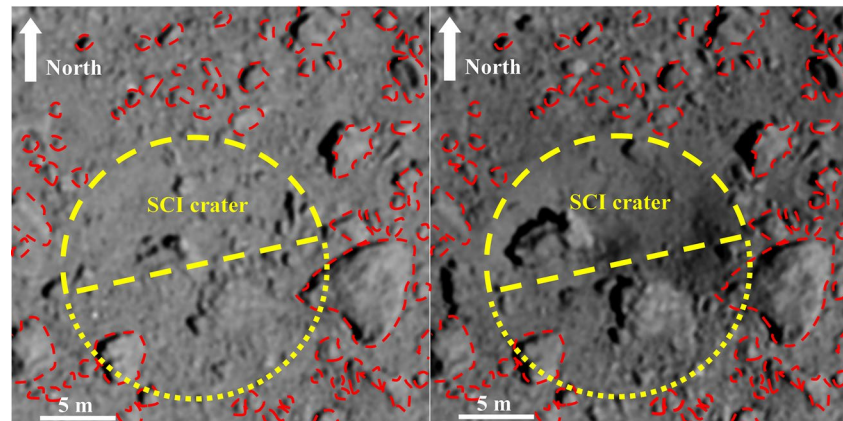


Figure 1. The images taken before (left) and after (right) the SCI impact by the ONC-Telescopic at an altitude of 1.7 km on March 21, 2019 and April 25, 2019, respectively. The SCI crater defined in Arakawa et al. (2020) is shown by a yellow dashed semicircle. We exclude the SCI crater and the area surrounded by the yellow dotted line from the analysis of the movement distance of the boulder because the cratering process likely has symmetrical effects around the impact pit. The edges of boulders before the SCI impact are shown by the red dashed lines in both images. In the post-SCI image, the lateral movement of the boulders excited by seismic waves is smaller than 1 m. Image source: http://www.darts.isas.jaxa.jp/pub/hayabusa2/paper/Arakawa_2020.

iSEM3D describes 3D structure by an axisymmetric 2D mesh with azimuthal expansion by Fourier series to simulate seismic wavefield with a lower calculation cost and shorter computation time than other numerical approaches, such as 3D SPEC-FEM modelings (Komatitsch & Tromp, 2002a, 2002b). This code simulates direct wave propagation, but not scattered wavefield. Garcia et al. (2015) describe the peak ground motion of the scattered wavefield in the vicinity of the SCI crater as expected to be smaller than that of the direct wave. To constrain the maximum horizontal movement of the surface material, we evaluate peak ground motion in numerical calculations, in which scattering is incorporated as an attenuation of the direct wave in the form of the quality factor. The strength of direct waves and a scattered wavefield are further examined as functions of distance in Section 5.

2.2. Asteroid Models

Britt et al. (2002) indicate that macroporosity inside asteroids is highly variable: rubble-pile asteroids, such as Mathilde, fractured ones, such as Eros, and coherent ones, such as Vesta. Such variation of internal structures could have a significant influence on rigidity, quality factor, and consequently elastic wave propagation. Therefore, we consider a wide ranges of mechanical properties from unconsolidated particles to solid rock.

For the numerical simulation, we first assume Poisson's ratio and density of Ryugu to be constant at 0.25 and $1,190 \text{ kg/m}^3$, respectively (Watanabe et al., 2019). Next, we set acceptable rigidity and quality factor ranges based on estimates from lunar seismic observations and laboratory experiments (Table 1). Because the rigidity of powder is generally smaller than that of consolidated rocks (Yuu et al., 1986), the rigidity of rubble-pile asteroids must be lower than $4 \times 10^{10} \text{ Pa}$ of the Preliminary Reference Earth Model (PREM) crust (Dziewonski & Anderson, 1981). Knapmeyer et al. (2018) show from the measurement of the sound speed of lunar regolith (Anderson et al., 1970; Tittmann & Houley, 1971) that the rigidity is higher than $\sim 1 \text{ MPa}$ in highly porous regolith and lower than $\sim 1 \text{ GPa}$ in packed regolith. Thus, we limit the rigidities of rubble pile asteroids between 1 MPa and 1 GPa. This range of rigidity is consistent with P wave velocities of the moon, which are $\sim 0.1 \text{ km/s}$ at the surface (Nakamura, 1976) and 0.5 km/s in the subsurface shallower than 1 km (Toksöz et al., 1974).

In this simulation, we also consider a wide quality factor range, which includes intrinsic absorption and scattering loss (Sato et al., 2012). Hereafter we call quality factors corresponding to intrinsic absorption and scattering loss $^I Q$ and $^{Sc} Q$, respectively, and define an effective quality factor $^E Q$ as

Table 1
Rigidities, Quality Factors and Seismic Efficiencies of Terrestrial and Lunar Material

Materials	Rigidity (Pa)	Materials	Quality factor (frequency range)	Condition	Seismic efficiency
Terrestrial crust (Dziewonski & Anderson, 1981)	4×10^{10}	Terrestrial crust (Dziewonski & Anderson, 1981)	${}^E Q_S = 600 (<1 \text{ Hz})$	Underground nuclear explosion (Patton & Walter, 1993)	$10^{-2} - 10^{-1}$
Lunar soil (Knapmeyer et al., 2018)	$10^6 - 10^9$	Lunar surface (Dainty et al., 1974; Nakamura, 1976)	${}^I Q_S = 2,000 - 5,000 (4-8 \text{ Hz})$	Impact experiment on loose sand (McGarr et al., 1969)	$10^{-6} - 10^{-5}$
Sand (Kimura & Kawashima, 1995)	7.42×10^6	Uncompressed sand (Daubar et al., 2018)	${}^E Q \sim 5 (\sim 1 \text{ kHz})$	Artificial impacts of Apollo 12 and 13 (Latham et al., 1970)	$10^{-6} - 10^{-5}$
Ranges used in Figures 2 and 3	$10^6 - 10^9$	Ranges used in Figures 2 and 3	${}^E Q_S = 5 - 5,000$	Ranges used in Figures 2 and 3	$10^{-6} - 10^{-4}$

$$\frac{1}{{}^E Q} = \frac{1}{{}^I Q} + \frac{1}{{}^{Sc} Q} \quad (1)$$

According to Dainty et al. (1974), ${}^I Q$ in the lunar surficial scattering layer is estimated to be 5,000, and Nakamura (1976) shows that the dissipation quality factor ranges from 1,600 to 2,300. The dissipation quality factor consists of anelastic attenuation and loss of seismic energy from surficial regolith to a deeper layer. Therefore, Nakamura (1976) concludes that ${}^I Q$ will be greater than 2,000.

${}^{Sc} Q$ has not been measured independently from ${}^I Q$ and always appears in ${}^E Q$. In previous laboratory experiments, ${}^E Q$ of unconsolidated sand is 5 (Daubar et al., 2018). This small ${}^E Q$ is likely dominated by ${}^{Sc} Q$. Thus, as two extreme cases of dominant ${}^I Q$ and ${}^{Sc} Q$, we set an upper bound and a lower bound of S wave ${}^E Q$, ${}^E Q_S$, as 5 and 5,000, respectively (Table 1). We assume for simplicity that P wave ${}^E Q$, ${}^E Q_P$, is fixed at $9/4 {}^E Q_S$ (Dziewonski & Anderson, 1981) and that quality factor is frequency independent. Although the intrinsic quality factor of the lunar mantle is proportional to frequency powered by 0.7 (Nakamura & Koyama, 1982), such a relationship has not been measured for regolith.

We also consider an inner structure of rubble pile asteroid, although observational constraints have not yet been obtained. Britt and Consolmagno (2001) indicate that, in rubble-pile asteroids, fine grains are confined near the surface, whereas large voids are at the center. Hirabayashi et al. (2015) report that asteroids with surface shedding have a strong core covered by fluffy surface materials. To evaluate the influence of inner structures on the maximum ground motion of the asteroid surface, we test three simple models: (i) the “rigid core” model, with a core covered by a soft shell, (ii) the “soft core” model, with a core covered by a rigid shell, and (iii) the “homogeneous” model. Sugita et al. (2019) report that no crater on Ryugu has been found to have a floor with a terrace structure, indicating that the strength contrast between the surface layer and the interior is negligible. The lower bound of the surface layer thickness is given by the depth of the largest crater on Ryugu, Urashima, which is ~ 45 m (Sugita et al., 2019). This lower bound is sufficiently large compared with the wavelength of the dominant surface wave as we explain in detail later. Therefore, we assume the thickness of the shells to be 50 m for the (i) rigid core and (ii) soft core models.

2.3. Seismic Source

The source moment tensor of impact-induced seismic wavefield has the same form as that of explosion and can be expressed by a diagonal matrix, \mathbf{M} . Teanby and Wookey (2011) yield the relationship between \mathbf{M} and kinetic energy of impactor, E_k , as

$$\mathbf{M} = \frac{\sqrt{2}}{\sqrt{3}} \begin{bmatrix} M_0 & 0 & 0 \\ 0 & M_0 & 0 \\ 0 & 0 & M_0 \end{bmatrix} \quad (2)$$

$$M_0 = \left(\frac{\epsilon E_k}{4.8 \times 10^{-9}} \right)^{\frac{1}{1.24}} \quad (3)$$

where ϵ is the seismic efficiency, namely, the conversion ratio of the kinetic energy of the impactor to seismic energy. The kinetic energy of SCI is 4.0×10^6 J that is calculated from the 2-kg mass of impactor and the 2-km/s velocity of the impact (Arakawa et al., 2017). In contrast, ϵ is highly uncertain because several experiments produce a wide range of estimates: from 10^{-2} to 10^{-1} in an underground nuclear explosion (Patton & Walter, 1993), from 10^{-6} to 10^{-4} in impact experiments on loose sand (McGarr et al., 1969), and from 10^{-6} to 10^{-5} in the artificial impacts of Apollo 12 and 13 boosters (Latham et al., 1970). Explosions and nuclear tests in bedrock or consolidated materials tend to have ϵ higher than 10^{-3} , whereas impacts on sediments and unbonded sand tend to have ϵ lower than 10^{-5} . A high attenuation during propagation through medium, such as sand, would make the measured seismic efficiency smaller than the actual value (Richardson et al., 2005). Matsue et al. (2020) suggest that measured seismic efficiencies could be the upper limit, because the energy of the measured wavefield may include a plastic wave component. Furthermore, ϵ has never been measured for regolith under microgravity conditions. Following previous researches on asteroids, where ϵ is 10^{-6} (Garcia et al., 2015; Murdoch et al., 2017) and 10^{-4} (Richardson et al., 2004), we first apply ϵ from 10^{-6} to 10^{-4} . Later in this study, we show that ϵ smaller than previous estimates are required from the actual SCI impact.

Seismic source duration is another parameter required for our wave propagation simulation and is scaled empirically from ground impact experiment. McGarr et al. (1969) propose a scaling function of seismic source duration, t_s , from impact experiments on sand as:

$$t_s = \left(\frac{8\pi^2 \times 0.384 S^2 m_p}{\rho_t V_p^3 \epsilon} \right)^{\frac{1}{3}} \approx 4.95 \times \left(\frac{m_p}{\rho_t V_p^3 \epsilon} \right)^{\frac{1}{3}} \quad (4)$$

where S is a ratio of the incident impulse to the impulse transferred to the target, V_p is the sound speed of target, ρ_t is the density of target, and m_p is the mass of the projectile. We assume S to be two following McGarr et al. (1969). Once t_s is determined, the source time function is assumed to be a Gaussian with a half-width of $t_s / 2$.

3. Results and Interpretations of Elastic Deformation

In principle, surface materials can be moved by seismic reverberation in two ways: downslope motion of regolith layer and movement of individual boulders. To evaluate ease of downslope motion, we use the slope factor of safety equation (Lambe & Whitman, 1979; Richardson et al., 2005, 2020), taking the slope at the SCI location of $\sim 11^\circ$, the thickness of the regolith layer of 1 m (Richardson et al., 2005), and a cohesion of 4 Pa (Watanabe et al., 2019) for the sake of conservative estimate. This evaluation shows that seismic acceleration needs to be greater than 10 times Ryugu gravity to destabilize the regolith layer, and a boulder can move by seismic acceleration larger than gravity. Therefore, boulder hopping is more likely to occur than the downslope motion of the regolith layer, and we use boulder hopping as a constraint on seismic shaking on Ryugu.

3.1. Seismic Parameters Constrained by Hayabusa2 SCI Experiment

Assuming an explosive seismic source, P and Rayleigh wave are generated simultaneously with impact (Figure 2a). In the 2-layer models (i) and (ii), PP and PS waves are generated at the boundary between the surface layer and the core. Additionally, Rayleigh wave dispersion is observed and gives strong constraints on the subsurface structure of the body. Thus, for terrestrial seismology, the waveform analysis constrains the structural boundaries inside the Earth. However, in the SCI experiment, no seismometers were installed

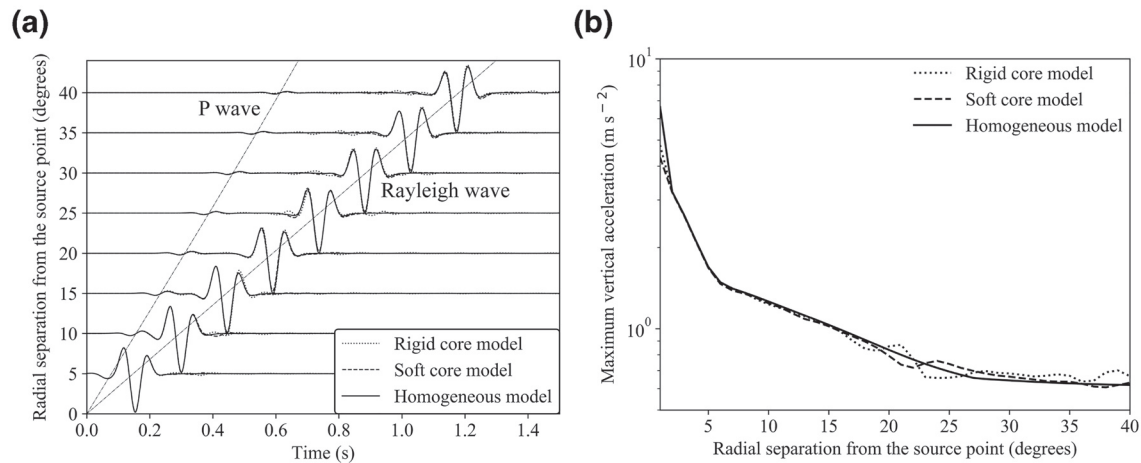


Figure 2. (a) Waveforms of three different models (rigid core (dotted line), soft core (dashed line), and homogeneous (solid line) model) and theoretical travel time of P and Rayleigh waves (dash-dot lines). (b) The maximum ground acceleration of the three models. Maximum vertical acceleration is calculated under the condition of the quality factor of 100 and seismic efficiency of 10^{-6} . The differences among (i) rigid core (dotted line), (ii) soft core (dashed line), and (iii) homogeneous (solid line) models are small.

on Ryugu; therefore, the waveform was not obtained. Instead, we concentrate only on the peak ground motion because the movement of boulders is controlled by the largest ground velocity.

Our simulations show that internal structure does not significantly affect impact-induced seismic acceleration in the tested cases. Maximum acceleration with respect to radial separation from the source in the three models, (i), (ii), and (iii), are compared in Figure 2b. For the “rigid core” model (dotted line), the core and surface rigidities are 10^9 Pa and 10^8 Pa, respectively. For the “soft core” model (dashed line), the core and surface rigidities are 10^7 Pa and 10^8 Pa, respectively. The homogeneous model has uniform rigidities of 10^8 Pa and is shown by a solid line. Figure 2b shows that the maximum amplitude of the seismic wave mostly depends on the surface property where Rayleigh waves propagate. In the range where radial separation is less than 40° , namely the source periphery, the maximum differences of acceleration are 28% and 35%, between “soft core” and “homogeneous” models, and “rigid core” and “homogeneous” models, respectively.

In our calculation, Figure 2a shows that the maximum amplitude of ground motion is governed by Rayleigh waves, which are dependent on the properties of shallow areas at depth of 0.2–0.4 of wavelengths for Poisson’s ratio of 0.25 (Soczkiewicz, 1997). This dependence of penetration depth on wavelength provokes wave dispersion; longer waves penetrate to deeper layers and vice versa. By taking ρ_t of $1,190 \text{ kg/m}^3$, m_p of 2 kg, and ϵ between 10^{-6} and 10^{-4} , we obtain t_s between 0.14 and 0.032 s. Then, the wavelength is between 52 and 11 m, and the penetration depth is always smaller than 50 m. Therefore, seismic shaking induced by the SCI impacts likely reflects the physical properties of the layer shallower than 50 m.

3.2. Results Based on Previously Estimated Parameters

The AxiSEM3D code calculates vertical and lateral ground velocities. When the maximum seismic acceleration exceeds the difference between universal gravitational and centrifugal force, the distance of lateral movement of the surface boulder can be calculated under the assumption that boulders are launched at the speed of ground velocity and hop along a parabolic orbit. At the location of the SCI impact, 7.9°N and 301.3°E , the net gravity is 0.12 mm/s^2 . Such calculated distance is a lower bound because subsequent bounces are not considered. Figure 3a illustrates the movement distance of boulders outside the SCI crater for a quality factor of 5 and the ranges of rigidity and seismic efficiency in Table 1. Figure 3a clearly demonstrates that the physical properties measured on the Moon and in laboratory experiments are not consistent with the limit of boulder movement distance less than 1 m on Ryugu. As previously suggested (e.g., Garcia et al., 2015), our numerical simulation indicates that surface velocity generated by the SCI impact is high enough to move boulders more than 1 m and, in most cases, higher than the escape velocity of the asteroid.

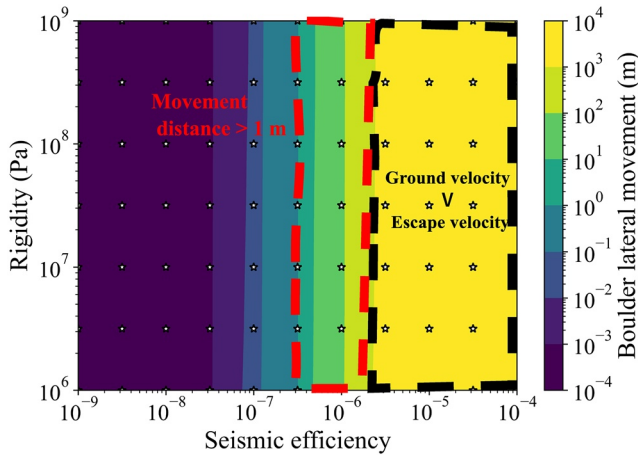


Figure 3. Lateral movement of boulders for variable seismic efficiency and rigidity (Table 1). The color shows the distances of lateral movement in the logarithmic scale. Every star shows the simulated models (see supporting information S1). In the case of ${}^E Q_S = 5$, the ground velocity exceeds the escape velocity of Ryugu, 37 cm/s, when ϵ is larger than 10^{-6} (the area enclosed with black dashed line). Or, the boulder movement distance is longer than 1 m, for ϵ between 3×10^{-7} and 10^{-6} (the area enclosed with red dashed lines).

To explain the absence of large boulder movement outside the SCI crater in Figure 1, we must consider extremely low values for the quality factor or seismic efficiency.

The quality factor that satisfies the 1-m constraint can be estimated given that the amplitude of displacement $A(\omega)$ decays with time as

$$A(\omega) = A_0(\omega) e^{-\frac{\omega t_{\text{travel}}}{2^E Q_R}} \quad (5)$$

where $A_0(\omega)$ is the amplitude of displacement without anelastic attenuation, ω is the angular frequency of the seismic wave, t_{travel} is the arrival time of Rayleigh wave, and ${}^E Q_R$ is the effective quality factor of Rayleigh wave. Through the Fourier transform of simulated wavefields, ${}^E Q_R$ satisfying boulder movement of less than 1 m is 0.5 or less for seismic efficiency larger than 10^{-6} (Table 1). Following the relationship between ${}^E Q_S$ and ${}^E Q_R$ (Aki and Richards, 1969), this upper bound of ${}^E Q_R$ can be translated into ${}^E Q_S$ less than 0.5.

We consider that such a low ${}^E Q_S$ cannot be validated for asteroid regolith. As described in Section 2, ${}^E Q_S$ includes an effect of scattering similarly to the coda waves of moonquakes, which is perhaps applicable to asteroid regolith. However, the viscous friction at the boundaries of grains damps little seismic waves without air or liquid. Tittmann (1977) shows that drying an olivine basalt results in low attenuation. Therefore, even if the direct waves are effectively attenuated, the amplitude of scattered waves

likely remains large and provokes regolith hopping as large as that present without scattering as we discuss in Section 5 in detail. Thus, scattering fails to satisfy the observational constraints.

4. Effect of Powdery Material under Microgravity Conditions

Little boulder movement on Ryugu is possibly explained by seismic efficiency lower than 3×10^{-7} . This energy conversion ratio from impact to seismic wave is consistent with Itokawa's value of $(1.0 \pm 0.5) \times 10^{-7}$ in crater erasure modeling by Richardson et al. (2020) but much smaller than the estimates in Table 1. Nevertheless, previous laboratory experiments on the compressional property of regolith suggest that the behavior of powdery material on Ryugu is indeed consistent with small seismic efficiency.

Our simulation assumes the elastic behavior of asteroid ground, but it is unclear if the loose powder like asteroid regolith behaves elastically. Images of the surface of Ryugu taken by Hayabusa2 and its mini landers show that the regolith consists of rocks in a wide range of size-frequency distribution (Michikami et al., 2019). The mechanical property of such regolith is not well understood but possibly assumed as an analog of powders. The powder behavior generally has plastic and elastic regimes (e.g., Yuu et al., 1986). The transition of the two regimes is determined by the yield strength of powder. When the stress is lower than the yield strength, the powder behaves like a solid in the elastic regime; the deformation propagates as seismic waves. When the stress exceeds the yield strength, the powder behaves plastically, causing efficient conversion of wave energy to plastic deformation. Because seismic stress can be calculated from the AxiSEM3D result, estimating the yield strength on asteroids and paying particular attention to interparticle force and structural effects is important.

Many types of interparticle force, such as self-gravity of particles, electronic force, radiation pressure, Van der Waals cohesion, and friction act on regolith. After careful evaluation of each force, Scheeres et al. (2010) indicate that the most effective interparticle force on asteroids is cohesion. Van der Waals cohesion of lunar regolith, P_c , is scaled by Sánchez and Scheeres (2014) as:

$$P_c[\text{Pa}] = \frac{0.011}{d[\text{m}]} \quad (6)$$

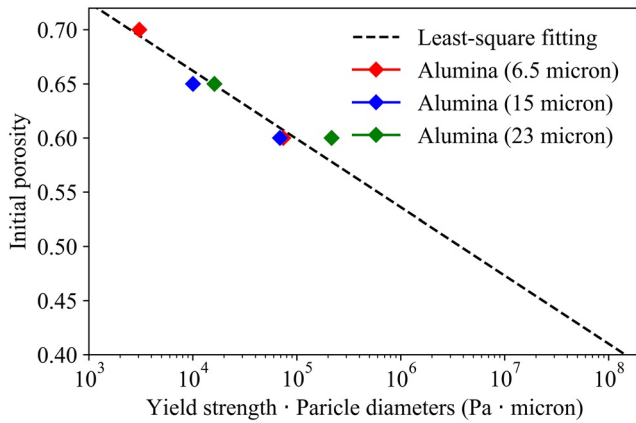


Figure 4. Relationship between the product of yield strength and particle diameter, and porosity. The dashed line is made by the least-square fitting to data (diamonds) taken from Table 3 from Omura and Nakamura (2017).

The above argument leads the yield strength, σ_Y , as proportional to the average cohesion of particles, P_c , with some modification due to porosity, ϕ

$$\sigma_Y = \alpha P_c f(\phi) \quad (7)$$

where $f(\phi)$ is a nondimensional function of porosity, and α is a constant value. Given that cohesion is inversely proportional to diameter, d , $\alpha f(\phi)$ is proportional to $d\sigma_Y$. Laboratory experiments by Omura and Nakamura (2017) imply that $f(\phi)$ could be a power law of porosity. Thus, we take six sets of alumina data in Table 3 from Omura and Nakamura (2017) and derive the following relationship (Figure 4):

$$d\sigma_Y = 10^{(-15.9 \pm 2.5)\phi + (8.4 \pm 1.6)} [Pa \cdot m] \quad (8)$$

We use alumina measurements, because its irregular shape is similar to impact fragments. From the above formula, we estimate that σ_Y is smaller than ~ 1 kPa; the macroporosity of Ryugu regolith is $\sim 46\%$, and grain size is more than 10 cm (Okada et al., 2020). Although the surface strength of Itokawa is estimated to be 10–20 kPa in crater erasure modeling (Richardson et al., 2020), Hirabayashi et al. (2019) propose based on finite element model simulations that cohesive strength must be between ~ 4 and 10 Pa to reproduce

deformation inside Ryugu, corresponding to sub-centimeter scale grains (Equation 6). Wada et al. (2018) estimate the tensile strength of Ryugu regolith as 1 kPa or less. Arakawa et al. (2020) estimated the cohesion strength of the subsurface layer to be between 140 and 670 Pa, based on the observation of the pit near the impact point. These estimates agree that σ_Y is smaller than 1 kPa.

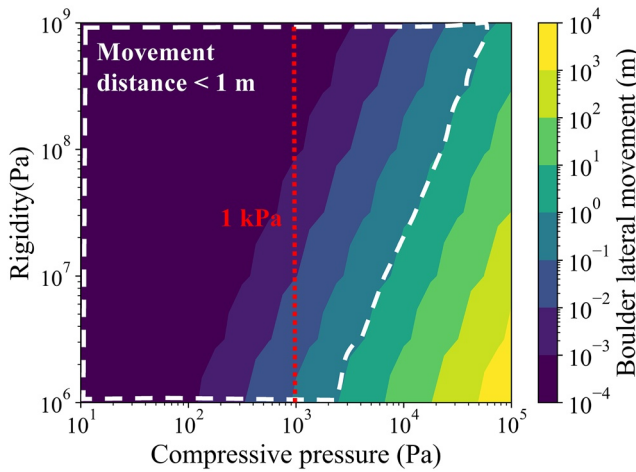


Figure 5. The lateral movement of boulders 8 m from the source location when $^E Q_S$ equals 5. The area enclosed by the white dashed line shows the range of parameters where the lateral regolith movement is smaller than 1 m. The red dotted line illustrates the transition between the elastic regime on the left-hand side and the plastic regime on the right-hand side for the case of 1 kPa yield strength.

Figure 5 shows the results of the AxiSEM3D simulation for $^E Q_S$ of 5. Lateral movement of boulders 8 m from the source location, that is, around the SCI crater rim, is shown by color contours. In contrast to Figure 3, the contours are drawn with respect to rigidity and calculated maximum compressive stress. Assuming that the yield strength is 1 kPa, the elastic wave can propagate only on the left side of the red dotted line where the seismic stress is smaller than 1 kPa. Figure 5 also shows that the lateral movement is always smaller than 1 m in the elastic regime, consistent with Figure 1.

To summarize, stress higher than yield strength results in the rapid conversion of kinetic energy to plastic deformation within the vicinity of the impact crater. Then, the apparent seismic efficiency of unconsolidated regolith becomes excessively small. After the kinetic energy dissipates sufficiently, the stress becomes lower than the yield strength. In this regime, the regolith layer behaves as an elastic body, enabling the seismic

waves to propagate. Thus, the low-yield strength expected on Ryugu limits the amplitude of ground motion, leading to the apparent lack of boulder motion outside the SCI crater in contrast to the general notion of effective seismic shaking on asteroids (Garcia et al., 2015).

5. Implication for Asteroid Resurfacing by Seismic Shaking

Figure 1 demonstrates that strong seismic shaking did not occur in the SCI experiment, but does not confirm that the surface of Ryugu is resistant to impacts of any size. On the contrary, the deficiency of small craters on Ryugu suggests an erosion of small-scale topography (Sugita et al., 2019). To estimate the seismic shaking effect on surface renewal on Ryugu, we need to extend our results to a whole spectrum of impactor sizes. For this purpose, we evaluate seismic acceleration at the surface. Once the local vertical seismic acceleration exceeds the difference of universal gravity and centrifugal force, the surface materials on an asteroid can be destabilized. This evaluation is different from the lateral movement that we calculate in Sections 3 and 4 but allows a direct comparison with previous works (e.g., Richardson et al., 2004). Furthermore, Quillen et al. (2019) propose a scaling of seismic acceleration to estimate the contribution of seismic reverberation. We aim to formulate a new seismic scaling by taking into account the effect of regolith yield strength.

Given that σ_Y limits the elastic wave generated by impacts, vertical ground acceleration at the surface can be combined with σ_Y in isotropic Poisson media, using seismic source duration shown in Equation 4. Using the analytical solution of two dimensional Rayleigh waves in a cartesian plane, vertical acceleration at the crater rim, a_0 , is derived approximately as:

$$a_0 = 1.1 \times \rho_t \frac{2}{3} m_p \frac{1}{3} \epsilon^3 \sigma_Y \quad (9)$$

where ρ_t is the target density, m_p is the projectile mass, and ϵ is the seismic efficiency (Appendix 1). The above scaling is different from that of Equations 16–18 in Richardson et al. (2020). Equation 9 of this study is based on the premise that seismic stress must be smaller than yield strength and that source time follows the scaling proposed by McGarr et al. (1969). Seismic pressure limitation has not been incorporated in previous researches, including Richardson et al. (2020). Considering the geometrical and anelastic energy dissipation of Rayleigh waves, the seismic acceleration, a_R , can be expressed as a function of separation from the epicenter to observation point, θ , as:

$$a_R(\theta) = a_0 \left(\frac{r_0}{R \sin \theta} \right)^{\frac{1}{2}} \exp \left(-1.2 \frac{\rho_t^{\frac{1}{3}} \epsilon^{\frac{1}{3}} (R\theta - r_0)}{m_p^{\frac{1}{3}} E Q} \right) \quad (10)$$

where R is the asteroid radius, and r_0 is the radial distance from the source where horizontal stress equals σ_Y , that is, approximately the crater radius (Appendix 1). Following the π -scaling in gravity regime reported by Arakawa et al. (2020), the crater radius made by an impactor at the speed of V_{impact} is

$$r_0 = 28 \times \rho_t^{-0.45} m_p^{0.28} V_{\text{impact}}^{0.34} R^{-0.17} \quad (11)$$

Richardson et al. (2020) indicate that coda waves generated by intense scattering medium are important for seismic shaking on a global scale. For moonquakes, a diffusion equation with frequency-dependent diffusivity is modeled by Nakamura (1976, 1977). In the case of the asteroid, Richardson et al. (2020) approximate seismic acceleration amplitude of coda waves depending on θ by assuming that the seismic energy propagates as a thin, hemispherical shell. Following Richardson et al. (2020), we derive the seismic acceleration of coda waves as

$$a_C(\theta) = \frac{a_0}{4} \left(\frac{r_0}{R \sin \frac{\theta}{2}} \right)^2 \exp \left(-\frac{2f \left(4R^2 \sin^2 \frac{\theta}{2} - r_0^2 \right)}{\xi \pi^l Q} \right) \quad (12)$$

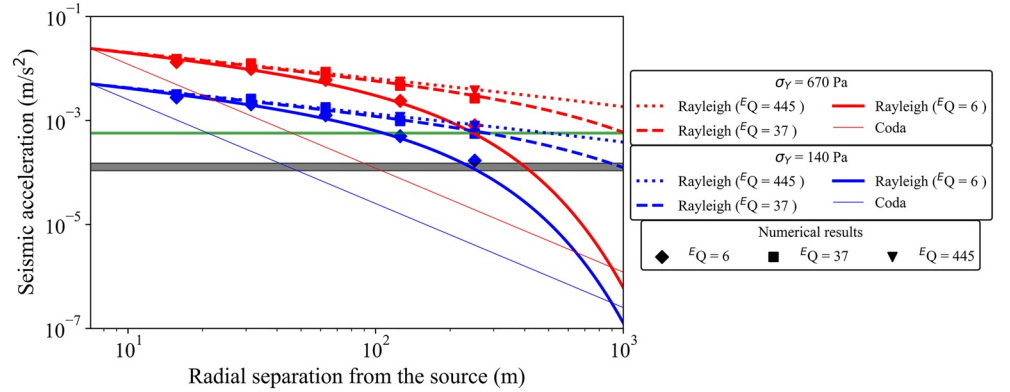


Figure 6. The vertical seismic acceleration with respect to radial distance for 9 cases. Red and blue lines show the cases for σ_γ of 670 and 140 Pa (upper and lower limits by Arakawa et al., 2020), respectively. Solid, dashed, and dotted lines show the cases of ${}^E Q_R = 6, 37,$ and $445,$ which correspond to ξ_0 of $0.03, 0.002,$ and $0.0003 \text{ km}^2/\text{s},$ respectively. The gray band is the net gravity value on Ryugu, and the green band is the seismic acceleration necessary for 10-cm boulder to hop against cohesion. Diamonds, squares, and triangles are numerical results. Thin solid lines correspond to the seismic acceleration caused by coda waves. The effect of ξ_0 on coda waves is small around the SCI crater. The difference of seismic acceleration between ξ_0 of 0.03 and $0.0003 \text{ km}^2/\text{s}$ is smaller than 10%. ϵ of 10^{-7} is assumed based on our results in Section 3.

where ξ is the diffusivity and f is the frequency. The diffusivity is dependent on the wavelength and size-distribution of subsurface scatterers. Then, assuming that the size distribution of subsurface scatterers is the same as that of boulders on Ryugu (Michikami et al., 2019), we can derive the dependence of ξ on f as follows:

$$\xi = \xi_0 \left(\frac{f}{f_0} \right)^{-1.65} \quad (13)$$

(Appendix 2). Additionally, the relationship between quality factors and diffusivity (e.g., Sato et al., 2012) is given by

$${}^{sc} Q = \frac{6\pi f \xi}{V_s^2} \quad (14)$$

In Figure 6, the seismic acceleration induced by the SCI impact is calculated for both direct Rayleigh waves and coda waves using the Equations from 9 to 14 for sets of different σ_γ and ξ_0 . Here, we assume ϵ of 10^{-7} based on our results in Section 3, ${}^I Q$ of 2,000, and V_s of 100 m/s as lunar surface regolith (Nakamura, 1976). The thick and thin lines show seismic acceleration by Rayleigh waves in Equation 10 and coda waves in Equation 12, respectively. ${}^E Q_S$ can be directly converted to ξ_0 using Equations 1, 13, and 14. For ${}^E Q_R$ between 6 and 445, the corresponding ξ_0 is between 0.03 and $0.0003 \text{ km}^2/\text{s}$. For this range of ξ_0 , calculated seismic accelerations are almost identical. To confirm the approximation of Equation 10, we show numerical calculation results by diamonds, triangles, and squares (Figure 6). An agreement between numerical results and our scaling of Rayleigh wave suggests that Rayleigh wave propagation is well-modeled by Equation 10. For comparison, the net gravity on Ryugu varies with latitude and is shown by the gray band in Figure 6. Based on the surface acceleration data by Watanabe et al. (2019), the net gravity of Ryugu ranges from 0.11 to 0.15 mm/s^2 at the current state of shape and rotation. In addition, the effect of cohesion needs to be taken into account for 10 cm particles (Okada et al., 2020) under microgravity condition. Considering the cohesion of 0.1 Pa , the necessary acceleration increases up to 0.6 mm/s^2 (green band in Figure 6). For particles larger than 1 m, the effect of cohesion is negligible.

The scaling of the Equation 10 has two important indications. First, the area affected by the seismic shaking of the SCI experiment is possibly dominated by Rayleigh waves. Nakamura (1976) estimates a ξ_0 of $0.03 \text{ km}^2/\text{s}$ in lunar regolith for f_0 of 4 Hz from signals from the moving lunar rovers. Richardson et al. (2020)

estimate frequency-independent ξ_0 at 0.002 km²/s for Itokawa from crater erasure modeling. For ξ_0 between 0.002 and 0.03 km²/s, Figure 6 shows that the seismic acceleration of Rayleigh wave exceeds that of coda waves at distances greater than 1,000 m on Ryugu, because the propagation distance in a sub-km-sized asteroid is so small that the direct wave overcomes scattered waves as described by Garcia et al. (2015).

Second, the effects of seismic modification extend up to, at least, a few hundred meters from the impact point. If the cohesion strength of the subsurface layer is between 140 and 670 Pa, as estimated by Arakawa et al. (2020), seismic acceleration excited by the SCI impact falls along the blue and red lines in Figure 6 and exceeds 0.6 mm/s² in the periphery of the SCI crater. Even if the $^E Q_R$ of six like fluffy sand (Daubar et al., 2018) is taken, seismic acceleration (solid lines) exceeds the 0.6 mm/s² criterion within the 100-m radius from the SCI crater, respectively. This result may seem inconsistent with Figure 4. However, even if the surface acceleration overcomes gravity and cohesion, lateral movement is negligible, because horizontal velocity is very small. Thus, although no evidence of boulders' hopping was found in Figure 1, modification smaller than image resolution is possible. Future investigation of pre- and post-SCI images may put a precise constraint on surface modification and limits rigidity and yield strength from movements of small boulders using Figure 5. Yield strength smaller than 4 Pa can explain no modification in the post-SCI image, because the seismic acceleration at the SCI crater rim is smaller than the net gravity level. According to the scaling relationship between yield strength and particle size in Equation 8, the particle size must be larger than 2 m for powdery media with the low-yield strength and the porosity of ~46 % such that on Ryugu. This size is an order of magnitude larger than the lower bound estimated from the surface thermal inertia (Okada et al., 2020).

By incorporating the size-frequency of impact flux, we can integrate an influence of surface modification on Ryugu for multiple impacts. The impact flux on Ryugu, $F(m_p)$, is given by

$$F(m_p) = P_i \times \left(R + \left(\frac{3\pi m_p}{4\rho_t} \right)^{\frac{1}{3}} \right)^2 \times N(m_p) \quad (15)$$

where P_i is the intrinsic collision probability and $N(m_p)$ is the size-frequency distribution of impactors. For Ryugu, we take $N(m_p)$ from the near-Earth asteroid (NEA) size distribution model (O'Brien & Greenberg, 2005; O'Brien et al., 2006). The asteroid size distribution is proportional to its size powered by -2.9 . The power law index is smaller than that of the crater size distribution on Ryugu (Sugita et al., 2019). We use P_i of $1.53 \times 10^{-23} \text{ m}^{-2} \text{ yr}^{-1}$ for NEA-NEA collisions (Bottke et al., 1994) and apply NEA values instead of those of the main belt, because the time scale of this study is much shorter than the dynamical NEA lifetime of typically a few Myr. Using this $F(m_p)$, the total area in which $a_R(\theta)$ or $a_C(\theta)$ exceeds the net gravity is calculated per year for given m_p in the same manner as in Figure 6. For Equation 11, we assume V_{imp} of NEA to be 18 km/s (Bottke et al., 1994). The interior of the crater is included in this calculation to incorporate all surfaces affected by an impact. We integrate the product of $F(m_p)$ and the area for m_p heavier than a certain mass. Dividing this integration by asteroid surface area, we obtain the cumulative ratio of the modified area (Figure 7a). For example, if ξ_0 equals 0.02 km²/s in Ryugu (thick solid line), projectiles heavier than 10-mg produce craters with a diameter of 0.5 m or larger. Thus, more than 1% of the surface is annually modified by local seismic shaking caused by such impacts.

Figure 7a indicates that seismic shaking is governed by numerous micrometeoroid impacts, which excites high-frequency seismic waves. Because acceleration is proportional to seismic frequency (Appendix 1), such impacts efficiently generate seismic acceleration. On the other hand, high-frequency waves are scattered rapidly and confined near the impact point, because diffusivity decreases inversely with f (Equation 11). Therefore, micrometeoroids excite strong seismic shaking only within the local area. In Figure 7a, the variation of net gravity over latitudes is neglected because of its insignificant effect on the cumulative modified area. The net gravity varies on Ryugu from 0.11 to 0.15 mm/s², resulting in a difference of cumulative modified area smaller than 10% that varies over several orders of magnitude. Neither the effect of cohesion is considered, because we are interested in meter scale boulders. The results shown in Figure 7a are markedly different from previous works, such as that of Richardson et al. (2020), who estimate that impactors of a few centimeters diameter can create a global seismic event on Itokawa under an assumed frequency-inde-

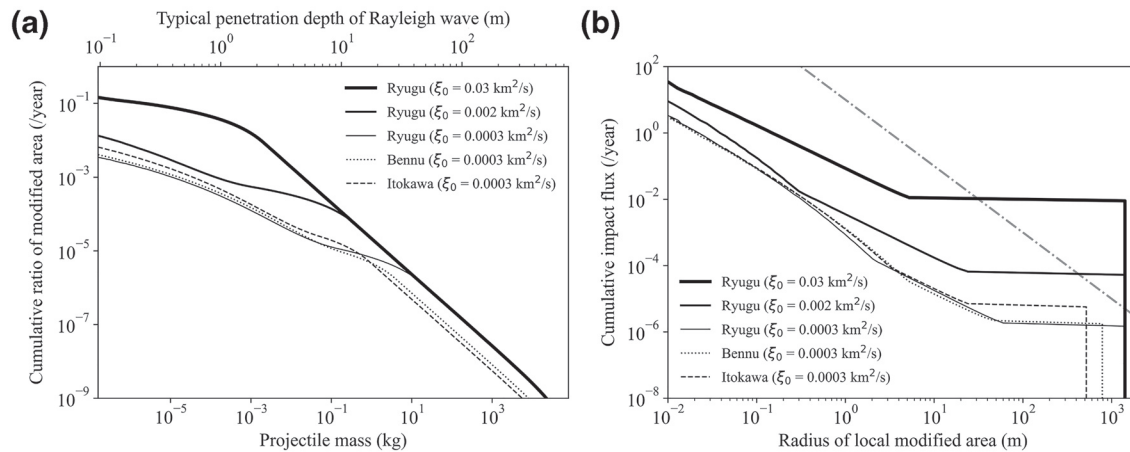


Figure 7. (a) Cumulative ratio of area modified by seismic shaking and crater formation as a function of projectile mass. The upper horizontal axis is the penetration depth of excited Rayleigh waves. (b) Size distribution of local seismic shaking area. The right end of each line becomes flat because every impact larger than a certain radius results in global seismic shaking on each asteroid. The gray dash-dot line illustrates a power law index of -2 .

pendent diffusivity of $0.002 \text{ km}^2/\text{s}$. The difference arises from our premise that seismic stress is limited by yield strength and our assumption that diffusivity depends on the seismic wavelength and size distribution of subsurface heterogeneities (Nakamura, 1976). We also note that the size of porous fragments on Ryugu is larger than 10 cm in diameter (Okada et al., 2020). Rayleigh waves with penetration depths shorter than this fragment size may not propagate. Thus, the horizontal axis in Figure 7b is truncated at this lower bound.

A comparison of Figure 7a with the findings of uncommon boulders constrains the diffusivity of Ryugu. The discovery of meter-sized boulders perched on other boulders (e.g., Figure 4d in Michikami et al., 2019) indicates that global seismic shaking does not occur frequently. This discovery suggests that diffusivity is small. For example, if lunar-like ξ_0 of $0.03 \text{ km}^2/\text{s}$ is assumed (thick solid line in Figure 7a), every projectile heavier than 1-g provokes global seismic shaking on Ryugu and occurs in ~ 10 years. However, the entire asteroid surface experiences seismic acceleration larger than gravity every 300 years if ξ_0 is $0.0003 \text{ km}^2/\text{s}$ (thin solid line in Figure 7a), because no micrometeoroid excites global seismic shaking. To sustain gravels isolated on boulders, the production of gravels must be faster than that of surface modification by seismic shaking. Kadono et al. (2020) report that the ejecta curtain of the SCI impact contains boulders of several decimeters. Therefore, craters with a radius of several meters are needed to generate gravels from impact ejecta. For example, according to Equations 10 and 14, a crater larger than 7 m in diameter is formed approximately every 300 years. Thus, ξ_0 must be lower than $0.0003 \text{ km}^2/\text{s}$ to be consistent with the existence of boulders on boulders. This value corresponds to ${}^E Q_R$ of six for the case of the SCI impact, which is almost the lower bound of ${}^E Q_R$ considered in numerical calculation.

Such a low diffusivity is two orders of magnitude smaller than estimates from lunar data analysis (Nakamura, 1976) but is possible if the difference of the regolith size is considered. As summarized by Papadakis (1968), scattered power by single heterogeneity of a diameter D is proportional to D^4 and D^6 in the Mie and Rayleigh scattering regimes, respectively. Considering the size difference between lunar and asteroid regolith, the intensity of scattering can change drastically with D for a given wavelength. Additionally, such low diffusivity is qualitatively consistent with a high attenuation rate estimated from seismic degradation on highly porous asteroids (Asphaug, 2008).

The prospect of absent global seismic shaking is challenged by the morphological differences among Ryugu, Benu, and Itokawa. Although Benu also has some boulders on boulders, no gravel isolated on top of boulders has been observed on Itokawa (Miyamoto et al., 2007). If they have the same elastic properties, the frequency of surface modification would be almost the same (thin solid line of Ryugu, dotted line of Benu, and dashed line of Itokawa in Figure 7a). Two possibilities can explain the morphological difference among these asteroids. First, the existence of a rigid core may cause the difference among small rub-

ble-pile asteroids. Although Ryugu appears homogeneous in the subsurface shallower than 50 m (Sugita et al., 2019), Itokawa has an area with a steep slope of $\sim 40^\circ$, which is proposed to be bedrock exposed on the surface (Barnouin-Jha et al., 2008). When the penetration depth of Rayleigh wave becomes deeper than the surface regolith layer, seismic shaking is dependent on properties of the deeper part below the regolith. To verify this possibility, we conduct numerical calculations for the impact of a 1-kg meteoroid on Itokawa. We assume that a rigid bedrock with ξ_0 of a few km^2/s is covered by regolith. Such a high ξ_0 is the same as lunar megaregolith (Dainty et al., 1974), corresponding to ${}^E Q_S$ of 5,000. ${}^E Q_S$ of regolith is 5. By changing the thickness of regolith to be 15, 10, and 5 m, the bulk ${}^E Q_S$ estimated from the maximum amplitude of ground motion becomes about 9, 12, and 24, respectively. Scattered body waves propagate through the core, and a broader area is affected by seismic shaking than on asteroids without a core. Qualitatively, long-lasting and strong global seismic shaking can be provoked by underlying rigid bedrock. The geomorphological difference among Itokawa, Bennu, and Ryugu may demonstrate that global seismic shaking signature may indicate the existence of a rigid core.

Second, we pay attention to size-frequency distribution of the area of local seismic shaking. The radius of the area of local seismic shaking can be calculated for a given m_p . Then, a plot of $F(m_p)$ with respect to the calculated radius shows the size distribution of the area of local seismic shaking. Circles of local seismic shaking areas are distributed randomly on asteroids like craters are spread over the lunar surface. This similarity suggests that global seismic shaking can be treated as an analogy of crater equilibrium (Melosh, 1989). If the index of power law relationship between the number and radius of the local seismic shaking circles is larger than -2 , global seismic shaking caused by large impact obliterates small ones and resets the cumulative effect. If this is the case, the cumulative modified area ratio shown in Figure 7a is useless, because global seismic shaking is regarded as stochastic process. Figure 7b shows the size distribution of local seismic shaking areas for variable ξ . The power law indexes are almost -2 or slightly larger, thus the difference of Ryugu and Itokawa can be inferred to be a result of the stochastic occurrence of large impacts. This possibility will be tested using returned samples from Ryugu brought back to the Earth in December 2020.

6. Conclusions

After the SCI operation in the Hayabusa2 mission, little surface modification was observed despite the prediction that strong seismic shaking efficiently transports surface material on asteroids (Garcia et al., 2015). To understand this unexpected observation, we conduct numerical simulations of seismic wave propagation on Ryugu by using a wide range of rigidities, quality factors, and seismic efficiencies with three types of inner structure models.

Our results show that maximum ground motion is mostly controlled by Rayleigh waves for the case of the SCI impact. Therefore, seismic wave propagation of regolith depends on surface properties. However, physical properties of regolith, which have been estimated from terrestrial experiments and moonquake observations, are not consistent with insignificant motion of boulders found in the comparison between the pre-SCI and the post-SCI images. We consider that asteroid regolith has either a quality factor or a seismic efficiency much lower than that of terrestrial and lunar analogs. In other words, seismic waves dissipate rapidly, or energy conversion from impact to seismic waves is small. The low-quality factor seems unlikely, because scattering cannot dissipate the total energy of waves under anhydrous condition. Additionally, low-yield strength is plausibly expected due to high porosity and weak forces between particles and likely causes extensive plastic deformation in the vicinity of the impact site, making the apparent seismic efficiency small.

Aiming to understand an influence of seismic shaking on small rubble-pile asteroids, we formulate seismic acceleration by Rayleigh and coda waves as a function of asteroid properties, such as density, size, and yield strength. Incorporating the impact flux on asteroid Ryugu, we estimate the frequency of surface modification by cratering and seismic shaking. To explain the existence of boulders perched on other boulders on Ryugu, we constrain diffusivity to be smaller than that of lunar regolith. Additionally, our estimates indicate that the existence and absence of such boulders on Ryugu and Itokawa can be attributed to a rigid core inside Itokawa or to a recent occurrence of stochastic global vibration.

Appendix 1: Scaling of Global Mobility due to Rayleigh wave

To evaluate the efficiency of global seismic shaking for various impactor masses and target asteroids, we derive the approximate formula of surface acceleration limited by yield strength. Our numerical simulation shows that maximum displacement at the surface is governed by Rayleigh waves (see Section 3). First, we derive seismic pressure stress generated by Rayleigh waves. For simplicity, we use the analytical solution of Rayleigh waves within a two-dimensional plane (e.g., Aki & Richards, 1969). The horizontal and vertical displacements of Rayleigh waves, u_x , and u_z , are:

$$u_x = Ak \exp(i(kx - \omega t) + \kappa_\alpha z) - 2A \frac{k\kappa_\alpha \kappa_\beta}{k^2 + \kappa_\beta^2} \exp(i(kx - \omega t) + \kappa_\beta z)$$

$$u_z = -iA\kappa_\alpha \exp(i(kx - \omega t) + \kappa_\alpha z) + 2Ai \frac{k^2 \kappa_\alpha}{k^2 + \kappa_\beta^2} \exp(i(kx - \omega t) + \kappa_\beta z)$$

where k is the wave number, ω is the frequency, and A is a constant. κ_α and κ_β are defined as $\kappa_\alpha^2 = k^2 - \left(\frac{\omega}{V_P}\right)^2$ and $\kappa_\beta^2 = k^2 - 3\left(\frac{\omega}{V_P}\right)^2$, respectively. The vertical acceleration at the surface is the second derivative of u_z with respect to t

$$\frac{\partial^2 u_z}{\partial t^2} \Big|_{z=0} = iA\omega^2 \frac{\kappa_\alpha \kappa_\beta^2 - k^2 \kappa_\alpha}{k^2 + \kappa_\beta^2} \exp(i(kx - \omega t))$$

At the free surface, σ_{zz} and σ_{xz} are 0 by definition. Only σ_{xx} has a finite value. In isotropic Poisson media,

$$\sigma_{xx} \Big|_{z=0} = \mu \left(3 \frac{\partial u_x}{\partial x} + \frac{\partial u_z}{\partial z} \right)$$

$$= iA\mu \frac{(3k^2 - \kappa_\alpha^2)(k^2 + \kappa_\beta^2) - 4k^2 \kappa_\alpha \kappa_\beta}{k^2 + \kappa_\beta^2} \exp(i(kx - \omega t))$$

where μ is the rigidity. Then we can relate $\frac{\partial^2 u_z}{\partial t^2}$ and σ_{xx}

$$\frac{\partial^2 u_z}{\partial t^2} \Big|_{z=0} = \frac{\omega^2}{\mu} \frac{\kappa_\alpha \kappa_\beta^2 - k^2 \kappa_\alpha}{(3k^2 - \kappa_\alpha^2)(k^2 + \kappa_\beta^2) - 4k^2 \kappa_\alpha \kappa_\beta} \sigma_{xx}$$

$$= \frac{\omega V_{\text{Rayleigh}}}{\mu} \frac{\frac{\kappa_\alpha}{k} \left(\frac{\kappa_\beta^2}{k^2} - 1 \right)}{\left(\left(3 - \frac{\kappa_\alpha^2}{k^2} \right) \left(1 + \frac{\kappa_\beta^2}{k^2} \right) - 4 \frac{\kappa_\alpha}{k} \frac{\kappa_\beta}{k} \right)} \sigma_{xx}$$

where $V_{\text{Rayleigh}} = \frac{\omega}{k}$. The dominant Rayleigh wave frequency corresponds to $2\pi / t_s$ and is given by Equa-

tion 3. In isotropic Poisson media, $\frac{\kappa_\alpha}{k} = 0.85$, $\frac{\kappa_\beta}{k} = 0.39$, and $\frac{V_P V_{\text{Rayleigh}}}{\mu} = \frac{1.6}{\rho}$, so

$$\begin{aligned}\frac{\partial^2 u_z}{\partial t^2} \Big|_{z=0} &= \frac{2\pi V_{\text{Rayleigh}}}{t_s \mu} \frac{\frac{\kappa_\alpha}{k} \left(\frac{\kappa_\beta^2}{k^2} - 1 \right)}{\left(\left(3 - \frac{\kappa_\alpha^2}{k^2} \right) \left(1 + \frac{\kappa_\beta^2}{k^2} \right) - 4 \frac{\kappa_\alpha}{k} \frac{\kappa_\beta}{k} \right)} \sigma_{xx} \\ &= 1.1 m_p^{-1/3} \rho_t^{-2/3} \varepsilon^{1/3} \sigma_{xx}\end{aligned}$$

For seismic shaking to occur in the elastic regime, σ_{xx} must be smaller than σ_Y . Otherwise, regolith deforms plastically. Thus, the vertical acceleration is written as

$$\frac{\partial^2 u_z}{\partial t^2} \Big|_{z=0} < 1.1 m_p^{-1/3} \rho_t^{-2/3} \varepsilon^{1/3} \sigma_Y = a_0$$

where a_0 is the vertical seismic acceleration at the rim of the crater. Similarly, $\partial^2 u_x / \partial t^2$ can be derived, and those solutions show that the vertical acceleration is ~ 1.5 times larger than the horizontal one.

Next, we consider the attenuation of energy due to propagation geometry and dissipation. The former is inversely proportional to the wavefront travel distance, and the latter is an exponential decay with travel time, t_{travel} . The total energy is proportional to the square of wave amplitude, and surface acceleration, a_R , is proportional to amplitude. Therefore,

$$\begin{aligned}a_R(\theta) &= a_0 \left(\frac{2\pi r_0}{2\pi R \sin \theta} \right)^{\frac{1}{2}} \exp\left(-\frac{\omega_0 t_{\text{travel}}}{2Q^E} \right) \\ &= a_0 \left(\frac{r_0}{R \sin \theta} \right)^{\frac{1}{2}} \exp\left(-\frac{\pi(R\theta - r_0)}{t_{\text{source}} Q^E V_{\text{Rayleigh}}} \right) \\ &= a_0 \left(\frac{r_0}{R \sin \theta} \right)^{\frac{1}{2}} \exp\left(-1.2 \frac{\rho_t^{\frac{1}{3}} \varepsilon^{\frac{1}{3}} (R\theta - r_0)}{Q^E m_p^{\frac{1}{3}}} \right)\end{aligned}$$

where θ is the separation of the observation point from the epicenter, r_0 is the crater radius, R is the radius of asteroid, ω_0 is the typical angular frequency, $2\pi / t_{\text{source}}$, and $^E Q$ is the effective quality factor.

Third, we estimate r_0 . On Ryugu, r_0 is governed by π -scaling in gravity regime (Arakawa et al., 2020).

$$\begin{aligned}\pi_R &= r_0 \left(\frac{\rho_t}{m_p} \right)^{\frac{1}{3}} \\ \pi_2 &= \frac{g_{\text{asteroid}} d_{\text{projectile}}}{V_{\text{impact}}^2} = \frac{\frac{4\pi}{3} G \rho_t R \left(\frac{3m_p}{4\pi\rho_t} \right)^{\frac{1}{3}}}{V_{\text{impact}}^2} = \frac{\frac{4\pi}{3} G \rho_t R \left(\frac{3m_p}{4\pi\rho_t} \right)^{\frac{1}{3}}}{V_{\text{impact}}^2} \\ &= 1.73 \times 10^{-10} V_{\text{impact}}^{-2} \rho_t^{\frac{2}{3}} R m_p^{\frac{1}{3}} \\ \pi_4 &= \frac{\rho_t}{\rho_{\text{projectile}}} \\ \pi_R &= 0.62 \pi_2^{-0.17} \pi_4^{0.0014}\end{aligned}$$

Assuming that the density of target body and projectile is same, the crater radius is

$$\begin{aligned} r_0 &= 0.62 \times \rho_t^{-\frac{1}{3}} m_p^{\frac{1}{3}} \times \left(1.73 \times 10^{-10} V_{\text{impact}}^{-2} \rho^{\frac{2}{3}} R m_p^{\frac{1}{3}} \right)^{-0.17} \\ &= 28 \times \rho_t^{-0.45} m_p^{0.28} V_{\text{impact}}^{0.34} R^{-0.17} \end{aligned}$$

Appendix 2: Dependence of Diffusivity on Frequency

The intensity of seismic scattering is dependent on the size of the scatterer relative to the dominant wavelength. Yoon (2005) describes the regime of scattering using a dimensionless parameter $2\pi D / \lambda$, where λ is the wavelength, and D is the size of the scatterer. If $2\pi D / \lambda < 0.01$, the seismic medium can be regarded as quasi-homogeneous, and scattering effects are negligibly small. If $2\pi D / \lambda > 0.01$, Rayleigh scattering occurs, and if $2\pi D / \lambda > 0.1$, incident waves are scattered with large angles due to Mie scattering.

Let us assume that an effective scatterer meets $2\pi D / \lambda > 0.01$ and the size distribution of scatterers larger than D is given by

$$N \propto D^{-b}$$

where N is the number per unit area of scatterers. Assuming that the size distribution of scatterers is the same as that of boulders, b is 2.65 (Michikami et al., 2019). Following the analysis by Nakamura (1976), seismic waves are regarded as particles traveling through a subsurface filled with scatterers. As the particles travel over distance Δx , the seismic wavefront is blocked by $N\Delta x$ scatterers. Its fraction, $F(\lambda)$, is described as:

$$\int_{\frac{0.01}{2\pi}\lambda}^{D_m} D \left\{ -\frac{d(N\Delta x)}{dD} \right\} dD = F(\lambda)\Delta x$$

where D_m is the largest scatterer size and

$$F(\lambda) \propto D_m^{1-b} - \left(\frac{0.01}{2\pi} \lambda \right)^{1-b}$$

Thus, the probability that seismic waves travels a distance x without scattering, $P(x)$, is

$$\begin{aligned} -dP(x) &= P(x)F(\lambda)dx \\ P(x) &= \exp(-xF(\lambda)) \end{aligned}$$

The above equations indicate that $F^{-1}(\lambda)$ is the mean free path of the scattering medium. The frequency-dependent diffusivity, $\xi(f)$, is the product of the seismic velocity and the mean free path. Thus, $\xi(f)$ can be expressed as

$$\xi(f) \propto \frac{1}{D_m^{-1.65} - \left(\frac{0.01}{2\pi} \lambda \right)^{-1.65}}$$

D_m can be taken as the size of Otohime boulder, 140 m, and λ excited by impacts is smaller than hundreds of meters (Figure 7a). Therefore, the first term of the numerator is negligible. By incorporating $\lambda = V_{\text{Rayleigh}} / f$, the frequency-dependent diffusivity is given as:

$$\xi(f) \propto f^{-1.65}$$

Data Availability Statement

The data used to produce Figure 1 may be downloaded from the Data ARchives and Transmission System (DARTS) of JAXA using the link (http://www.darts.isas.jaxa.jp/pub/hayabusa2/paper/Arakawa_2020). The numerical results and input data used to produce Figures 2, 3, 5 and 6 may be downloaded from the Mendeley Data repository (Nishiyama, 2020). The AxiSEM3D source code developed by Leng et al. (2016) can be acquired through the url (<https://github.com/kuangdai/AxiSEM3D>).

Acknowledgments

The authors are grateful to James E. Richardson and another anonymous reviewer for thorough and thoughtful comments. Also, the authors thank Erik Asphaug for providing helpful comments for an early draft of the manuscript. This work is supported by UGRASP 2018 and IGPEES, WINGS Program, the University of Tokyo, the Publication Committee of National Astronomical Observatory of Japan, and the JSPS Core-to-Core program "International Planetary Network." The authors would like to thank Editage (www.editage.com) for English language editing.

References

Aki, K., & Richards, P. G. (1969). *Quantitative seismology* (2nd ed.). Herndon: University Science Books.

Anderson, O. L., Scholz, C., Soga, N., Warren, N., & Schreiber, E. (1970). Elastic properties of a micro-breccia, igneous rock and lunar fines from Apollo 11 mission (pp. Vol. 3). *Proceeding the Apollo 11 lunar science conference*.

Arakawa, M., Saiki, T., Wada, K., Ogawa, K., Kadono, T., Shirai, K., et al. (2020). An artificial impact on the asteroid (162173) Ryugu formed a crater in the gravity-dominated regime. *Science*, 368(6486), 67–71. <https://doi.org/10.1126/science.aaz1701>

Arakawa, M., Wada, K., Saiki, T., Kadono, T., Takagi, Y., Shirai, K., et al. (2017). Scientific objectives of Small Carry-on Impactor (SCI) and Deployable Camera 3 Digital (DCAM3-D): Observation of an ejecta curtain and a crater formed on the surface of Ryugu by an artificial high-velocity impact. *Space Science Reviews*, 208(1), 187–212. <https://doi.org/10.1007/s11214-016-0290-z>

Asphaug, E. (2008). Critical crater diameter and asteroid impact seismology. *Meteoritics & Planetary Science*, 43(6), 1075–1084. <https://doi.org/10.1111/j.1945-5100.2008.tb00694.x>

Barnouin-Jha, O. S., Cheng, A. F., Mukai, T., Abe, S., Hirata, N., Nakamura, R., et al. (2008). Small-scale topography of 25143 Itokawa from the Hayabusa laser altimeter. *Icarus*, 198(1), 108–124. <https://doi.org/10.1016/j.icarus.2008.05.026>

Bottke, Jr, W. F., Nolan, M. C., Greenberg, R., & Kolvoord, R. A. (1994). Velocity distribution among colliding asteroids. *Icarus*, 107(2), 255–268. <https://doi.org/10.1006/icar.1994.1021>

Britt, D. T., & Consolmagno, S. J. G. J. (2001). Modeling the structure of high porosity asteroids. *Icarus*, 152(1), 134–139. <https://doi.org/10.1006/icar.2001.6628>

Britt, D. T., Yeomans, D., Housen, K., & Consolmagno, G. (2002). Asteroid density, porosity, and structure. In W. F. Bottke, Jr., A. Cellino, P. Paolicchi, & R. P. Binzel (Eds.), *Asteroids III* (pp. 485–500). Tucson: University of Arizona Press.

Colwell, J. E., Gulbis, A. A. S., Horányi, M., & Robertson, S. (2005). Dust transport in photoelectron layers and the formation of dust ponds on Eros. *Icarus*, 175(1), 159–169. <https://doi.org/10.1016/j.icarus.2004.11.001>

Dainty, A. M., Toksöz, M. N., Anderson, K. R., Pines, P. J., Nakamura, Y., & Latham, G. (1974). Seismic scattering and shallow structure of the Moon in oceanus procellarum. *The Moon*, 9, 11–29. <https://doi.org/10.1007/BF00565388>

Daubar, I., Lognonné, P., Teanby, N., Miljkovic, K., Stevanović, J., Vaubaillon, J., et al. (2018). Impact-seismic investigations of the InSight mission. *Space Science Reviews*, 214(8), 1–68. <https://doi.org/10.1007/s11214-018-0562-x>

Dziewonski, A. M., & Anderson, D. L. (1981). Preliminary reference Earth model. *Physics of the Earth and Planetary Interiors*, 25(4), 297–356. [https://doi.org/10.1016/0031-9201\(81\)90046-7](https://doi.org/10.1016/0031-9201(81)90046-7)

García, R. F., Murdoch, N., & Mimoun, D. (2015). Micro-meteoroid seismic uplift and regolith concentration on kilometer scale asteroids. *Icarus*, 253, 159–168. <https://doi.org/10.1016/j.icarus.2015.02.014>

Hirabayashi, M., et al. (2019). The western bulge of 162173 Ryugu formed as a result of a rotationally driven deformation process. *The Astrophysical Journal Letters*, 874, L10.

Hirabayashi, M., Sánchez, D. P., & Scheeres, D. J. (2015). Internal structure of asteroids having surface shedding due to rotational instability. *The Astrophysical Journal*, 808(1), 63. <https://doi.org/10.1088/0004-637X/808/1/63>

Kadono, T., Arakawa, M., Honda, R., Ishibashi, K., Ogawa, K., Sakatani, N., et al. (2020). Impact experiment on asteroid (162173) Ryugu: Structure beneath the impact point revealed by in situ observations of the ejecta curtain. *Astrophysical Journal Letters*, 899(1), L22. <https://doi.org/10.3847/2041-8213/aba949>

Kameda, S., Suzuki, H., Cho, Y., Koga, S., Yamada, M., Nakamura, T., et al. (2015). Detectability of hydrous minerals using ONC-T camera onboard the Hayabusa2 spacecraft. *Advances in Space Research*, 56(7), 1519–1524. <https://doi.org/10.1016/j.asr.2015.06.037>

Kameda, S., Suzuki, H., Takamatsu, T., & Sugita, S. (2017). Preflight calibration test results for Optical Navigation Camera Telescope (ONC-T) onboard the Hayabusa2 spacecraft. *Space Science Reviews*, 208(1), 17–31. <https://doi.org/10.1007/s11214-015-0227-y>

Kimura, M., & Kawashima, S. (1995). Study on physical parameters of the Biot-Stoll marine sediment model. *The Journal of the Marine Acoustics Society of Japan*, 22(1), 54–63 (in Japanese). <https://doi.org/10.1250/ast.28.230>

Knappmeyer, M., Fischer, H.-H., Knollenberg, J., Seidensticker, K. J., Thiel, K., Arnold, W., et al. (2018). Structure and elastic parameters of the near surface of Abydos site on comet 67P/Churyumov-Gerasimenko, as obtained by SESAME/CASSE listening to the MUPUS insertion phase. *Icarus*, 310, 165–193. <https://doi.org/10.1016/j.icarus.2017.12.002>

Komatitsch, D., & Tromp, J. (2002a). Spectral-element simulations of global seismic wave propagation—I. Validation. *Geophysical Journal International*, 149(2), 390–412. <https://doi.org/10.1046/j.1365-246X.2002.01653.x>

Komatitsch, D., & Tromp, J. (2002b). Spectral-element simulations of global seismic wave propagation—II. Three-dimensional models, oceans, rotation and self-gravitation. *Geophysical Journal International*, 150(1), 303–318. <https://doi.org/10.1046/j.1365-246X.2002.01716.x>

Lambe, T. W., & Whitman, R. V. (1979). *Soil mechanics* (SI ed.). New York, NY: Wiley & Sons.

Latham, G., Ewing, M., Dorman, J., Press, F., Toksöz, N., Sutton, G., et al. (1970). Seismic data from man-made impacts on the Moon. *Science*, 170(3958), 620–626. <https://doi.org/10.1126/science.170.3958.620>

Leng, K., Nissen-Meyer, T., & van Driel, M. (2016). Efficient global wave propagation adapted to 3-D structural complexity: A pseudospectral/spectral-element approach. *Geophysical Journal International*, 207(3), 1700–1721. <https://doi.org/10.1093/gji/ggw363>

Matsue, K., Yasui, M., Arakawa, M., & Hasegawa, S. (2020). Measurements of seismic waves induced by high-velocity impacts: Implications for seismic shaking surrounding impact craters on asteroids. *Icarus*, 338, 113520. <https://doi.org/10.1016/j.icarus.2019.113520>

McGarr, A., Latham, G. V., & Gault, D. E. (1969). Meteoroid impacts as sources of seismicity on Moon. *Journal of Geophysical Research*, 74(25), 5981–5994. <https://doi.org/10.1029/JB074i025p05981>

Melosh, H. J. (1989). *Impact cratering: A Geologic process* (pp. 253). New York, NY: Oxford Univ. Press.

- Michikami, T., Honda, C., Miyamoto, H., Hirabayashi, M., Hagermann, A., Irie, T., et al. (2019). Boulder size and shape distributions on asteroid Ryugu. *Icarus*, 331, 179–191. <https://doi.org/10.1016/j.icarus.2019.05.019>
- Miyamoto, H., Yano, H., Scheeres, D. J., Abe, S., Barnouin-Jha, O., Cheng, A. F., et al. (2007). Regolith migration and sorting on asteroid Itokawa. *Science*, 316(5827), 1011–1014. <https://doi.org/10.1126/science.1134390>
- Murdoch, N., Hempel, S., Pou, L., Cadu, A., Garcia, R. F., Mimoun, D., et al. (2017). Probing the internal structure of the asteroid Didymos with a passive seismic investigation. *Planetary and Space Science*, 144, 89–105. <https://doi.org/10.1016/j.pss.2017.05.005>
- Nakamura, Y. (1976). Seismic energy transmission in the lunar surface zone determined from signals generated by movement of Lunar Rovers. *Bulletin of the Seismological Society of America*, 66(2), 593–606.
- Nakamura, Y. (1977). Seismic energy transmission in an intensively scattering environment. *Journal of Geophysics*, 43, 1389–1399. Retrieved from <https://journal.geophysicsjournal.com/JofG/article/view/90>
- Nakamura, Y., & Koyama, J. (1982). Seismic Q of the lunar upper mantle. *Journal of Geophysical Research*, 87(B6), 4855–4861. <https://doi.org/10.1029/JB087iB06p04855>
- Nishiyama, G. (2020). *Nishiyama_et_al_2020* (Vol. 1). Mendeley Data. <https://doi.org/10.17632/6j2vj7w7d.1>
- O'Brien, D. P., & Greenberg, R. (2005). The collisional and dynamical evolution of the main-belt and NEA size distributions. *Icarus*, 178(1), 179–212. <https://doi.org/10.1016/j.icarus.2005.04.001>
- O'Brien, D. P., Greenberg, R., & Richardson, J. E. (2006). Craters on asteroids: Reconciling diverse impact records with a common impacting population. *Icarus*, 183(1), 79–92. <https://doi.org/10.1016/j.icarus.2006.02.008>
- Okada, T., Fukuhara, T., Tanaka, S., Taguchi, M., Arai, T., Senshu, H., et al. (2020). Highly porous nature of a primitive asteroid revealed by thermal imaging. *Nature*, 579(7800), 518–522. <https://doi.org/10.1038/s41586-020-2102-6>
- Omura, T., & Nakamura, A. M. (2017). Experimental study on compression property of regolith analogues. *Planetary and Space Science*, 149, 14–22. <https://doi.org/10.1016/j.pss.2017.08.003>
- Papadakis, E. P. (1968). Ultrasonic attenuation caused by scattering in polycrystalline media. *Physical Acoustics*, 4, 269–328. <https://doi.org/10.1016/B978-0-12-395664-4.50018-3>
- Patton, H. J., & Walter, W. R. (1993). Regional moment: magnitude relations for earthquakes and explosions. *Geophysical Research Letters*, 20(4), 277–280. <https://doi.org/10.1029/93GL00298>
- Quillen, A. C., Zhao, Y., Chen, Y., Sánchez, P., Nelson, R. C., & Schwartz, S. R. (2019). Impact excitation of a seismic pulse and vibrational normal modes on asteroid Bennu and associated slumping of regolith. *Icarus*, 319, 312–333. <https://doi.org/10.1016/j.icarus.2018.09.032>
- Richardson, J. E., Melosh, H. J., & Greenberg, R. (2004). Impact-induced seismic activity on asteroid 433 Eros: A surface modification process. *Science*, 306(5701), 1526–1529. <https://doi.org/10.1126/science.1104731>
- Richardson, J. E., Melosh, H. J., Greenberg, R. J., & O'Brien, D. P. (2005). The global effects of impact-induced seismic activity on fractured asteroid surface morphology. *Icarus*, 179(2), 325–349. <https://doi.org/10.1016/j.icarus.2005.07.005>
- Richardson, J. E., Steckloff, J. K., & Minton, D. A. (2020). Impact-produced seismic shaking and regolith growth on asteroids 433 Eros, 2867 Steins, and 25143 Itokawa. *Icarus*, 347, 113811. <https://doi.org/10.1016/j.icarus.2020.113811>
- Sánchez, P., & Scheeres, D. J. (2014). The strength of regolith and rubble pile asteroids. *Meteoritics & Planetary Science*, 49(5), 788–811. <https://doi.org/10.1111/maps.12293>
- Sato, H., Fehler, M. C., & Maeda, T. (2012). *Seismic wave propagation and scattering in the heterogeneous Earth*. Berlin Heidelberg: Springer Science & Business Media.
- Scheeres, D. J., Hartzell, C. M., Sánchez, P., & Swift, M. (2010). Scaling forces to asteroid surfaces: The role of cohesion. *Icarus*, 210(2), 968–984. <https://doi.org/10.1016/j.icarus.2010.07.009>
- Soczkiwicz, E. (1997). The penetration depth of the Rayleigh surface waves. *Nondestructive Testing and Evaluation*, 13(2), 113–119. <https://doi.org/10.1080/02780899708953022>
- Sugita, S., Honda, R., Morota, T., Kameda, S., Sawada, H., Tatsumi, E., et al. (2019). The geomorphology, color, and thermal properties of Ryugu: Implications for parent-body processes. *Science*, 364(6437), 252. <https://doi.org/10.1126/science.aaw0422>
- Teanby, N. A., & Wookey, J. (2011). Seismic detection of meteorite impacts on Mars. *Physics of the Earth and Planetary Interiors*, 186(1), 70–80. <https://doi.org/10.1016/j.pepi.2011.03.004>
- Thomas, P. C., Joseph, J., Carcich, B., Veverka, J., Clark, B. E., Bell, J. F., et al. (2002). Eros: Shape, topography, and slope processes. *Icarus*, 155(1), 18–37. <https://doi.org/10.1006/icar.2001.6755>
- Tittmann, B. R. (1977). Lunar rock Q in 3000–5000 range achieved in laboratory. *Philosophical Transactions of the Royal Society of London – Series A: Mathematical and Physical Sciences*, 285(1327), 475–479. <https://doi.org/10.1098/rsta.1977.0090>
- Tittmann, B. R., & Houley, B. R. (1971). Surface elastic wave propagation studies in lunar rocks. *Proceeding the 2nd Lunar Science Conference*, 3, 2337–2343.
- Toksöz, M. N., Dainty, A. M., Solomon, S. C., & Anderson, K. R. (1974). Structure of the Moon. *Reviews of Geophysics*, 12(4), 539–567. <https://doi.org/10.1029/RG012i004p00539>
- Tsubaki, J. (1984). New interpretation and application of Rumpf equation. *Journal of the Society of Powder Technology, Japan*, 21, 30–39 (in Japanese).
- Veverka, J., Thomas, P. C., Robinson, M., Murchie, S., Chapman, C., Bell, M., et al. (2001). Imaging of small-scale features on 433 Eros from NEAR: Evidence for a complex regolith. *Science*, 292(5516), 484–488. <https://doi.org/10.1126/science.1058651>
- Wada, K., Grott, M., Michel, P., Walsh, K. J., Barucci, A. M., Biele, J., et al. (2018). Asteroid Ryugu before the Hayabusa2 encounter. *Progress in Earth and Planetary Science*, 5(1), 1–30. <https://doi.org/10.1186/s40645-018-0237-y>
- Watanabe, S., Hirabayashi, M., Hirata, N., Hirata, N., Noguchi, R., Shimaki, Y., et al. (2019). Hayabusa2 arrives at the carbonaceous asteroid 162173 Ryugu-A spinning top-shaped rubble pile. *Science*, 364(6437), 268–272. <https://doi.org/10.1126/science.aav8032>
- Yasui, M., Matsumoto, E., & Arakawa, M. (2015). Experimental study on impact-induced seismic wave propagation through granular materials. *Icarus*, 260, 320–331. <https://doi.org/10.1016/j.icarus.2015.07.032>
- Yoon, M. (2005). *Deep seismic imaging in the presence of a heterogeneous overburden—Numerical modelling and case studies from the Central Andes and Southern Andes*. PhD, Freie Universität Berlin. [https://doi.org/10.1016/0926-9851\(93\)90007-L](https://doi.org/10.1016/0926-9851(93)90007-L)
- Yuu, S., Nakamura, S., & Furusawa, T. (1986). The stress-strain relationship in powder. *Journal of the Society of Powder Technology, Japan*, 23(12), 882–888 (in Japanese).